Origin of Chemisorption Energy Scaling Relations over Perovskite Surfaces

Yang Li,[a] Wei Cheng,[a] Zhi-Jun Sui,[a] Xing-Gui Zhou,[a] De Chen,[b] Wei-Kang Yuan,[a] Yi-An Zhu*[a]

[a]United Chemical Reaction Engineering Research Institute (UNILAB), State Key Laboratory of Chemical Engineering, East China University of Science and Technology, Shanghai 200237, China

[b]Department of Chemical Engineering, Norwegian University of Science and Technology, N-7491 Trondheim, Norway

ABSTRACT: Rationally tailored perovskites ABO_3 are promising substitutes for expensive noble-metal catalysts in heterogeneous catalysis. In this contribution, the BEEF-vdW+U method has been used to examine the adsorption of H, C, O, and CH_3 over (K, Rb, Cs, Sr, and Ba)BO_3 (B = d-block transition metals) and $ARuO_3$ (A = La - Ho) with various crystal structures. The calculated chemisorption energy of the simple species at the O site scales well with the surface oxygen vacancy formation energy of all the perovskites under consideration while the trend in the chemisorption energy at the B site can be described by the surface metal vacancy formation energy only over $ARuO_3$. Electronic structure analysis indicates that the perovskites could be classified into several categories according to the splitting and filling of the d and f orbitals of the B- and A-site cations, respectively. In each category, the chemisorption energies at the B site on (K,Rb,Cs,Sr,Ba)BO_3 and $ARuO_3$ are also closely related to the strength of the ionic bonding in the perovskites. Hence, the surface oxygen vacancy formation energy can be used as a descriptor to explain the trend in the calculated adsorption energies upon substitution of either B- or A-site cations, which has its origin in the fact that the larger the actual partial charges the oxygen and transition-metal ions carry, the stronger the B-O bond, which in turn weakens and enhances the ability of the O anions to withdraw and the ability of the B cations to donate electrons to the adsorbates, respectively.

I INTRODUCTION

Perovskites have been intensively investigated over the last few decades as one of the most promising materials applied in solid oxide fuel cells (SOFCs)[1], high-temperature oxygen sensors[2], oxygen sources in membrane separation[3], and heterogeneous catalysis[4]. In particular, rationally tailored perovskites are potential substitutes for expensive noble-metal catalysts[5]. On the one hand, perovskites can be used as catalysts under harsh conditions[6-8] because of their structural flexibility and stability at high temperatures. On the other hand, perovskites have comparable catalytic performance to noble metals but are much less costly. For instance, Ru-doped $SrTiO_3$[8] and $LaNi_{1-x}Mn_xO_3$ perovskite-type oxides[9] are reported to be able to attain a high conversion and a high selectivity with negligible amounts of carbon deposited in dry reforming of methane. As another example, $LaFeO_3$ can be used as the catalysts for the partial oxidation of methane by chemical looping to achieve a high selectivity toward synthesis gas.[10]

However, although there are several perovskites that prove catalytically active for specific reactions, it is not yet clear how to tailor the physical and chemical properties of perovskites to a particular chemical reaction. Perovskites were reported to show many tunable properties such as lattice distortion, magnetic property, electrical conductivity, thermal stability and chemical reactivity,[11] which originates from the great diversity of the composition and structure of perovskites with a general formula ABO_3. The A-site cations usually come from alkalis, alkaline earth, and rare earth metals, and B-site cations can be almost all the d-block transition metals cations.[5] The effect of electronic structures on the physicochemical properties of perovskites is sophisticated and of great importance.

To design a suitable catalyst for a given heterogeneous catalytic reaction, chemisorption energies of the simple species on catalyst surfaces have routinely been used as a descriptor to explain the trend in catalytic activity and selectivity. Experimentally, chemisorption energies can be obtained by measuring the rate of desorption or the temperature increase of a surface when it is covered by adsorbates[12]. However, experimental data alone sometimes are not sufficient to elucidate the effect of electronic structures on the catalytic performance of materials with different compositions and surface structures. Under these circumstances, DFT calculations can be performed to calculate chemisorption energies and activation energies, and several scaling relations between them have been established. The concept of the scaling relations can be traced back to the well-known Brønsted–

Evans–Polanyi (BEP) relationship[13-15] between activation energies and reaction energies. Based on the BEP relationship, transition state energy scaling relations are then developed to correlate the activation energy to a single adsorption energy[16-18], making the adsorption energy a key quantity in heterogeneous catalysis. To further reduce the number of independent catalytic parameters to be considered and to examine the nature of the scaling relations, chemisorption energy scaling relations are established[19-23]. By calculating the chemisorption energies of CH_x, OH_x, NH_x, and SH_x on different transition-metal surfaces, Abild-Pedersen et al.[19] found that the scaling relations can be explained in terms of the d-band model. Calle-Vallejo et al.[23] also correlated the adsorption energies of oxygenates to that of oxygen on various transition-metal surfaces, and suggested that the slope of the straight lines is closely related to the number of valence electrons of the atom bound to the surface.

Several attempts have previously been made to establish the chemisorption energy scaling relations over perovskite surfaces and to examine the electronic origin of their different adsorption properties. It was found that the adsorption behaviors of perovskite surfaces differ slightly from those of transition-metal surfaces. Montoya et al.[24] obtained the scaling relations between the chemisorption energies of H, O, and OH on the surfaces of a large number of cubic perovskites and suggested that a plausible descriptor could be the surface oxygen p-band center rather than the metal d-band center. Calle-Vallejo et al.[25-26] also found the formation energy of oxides is a remarkable descriptor of the surface reactivity of Sr- and La-based perovskites because both properties are strongly dependent on the number of valence electrons of the transition-metal cations.

Despite these many studies, little attention has been given to the adsorption behaviors of carbon-containing species over perovskites, and the majority of the previous DFT studies are conducted without removing the error in the computational method, e.g., the delocalization error (previously referred to as the "self-interaction error")[27]. These deficiencies may lead to inaccurate predictions about the trends in chemisorption energy on perovskites, which was discussed by Lee et al.[28]. Furthermore, the physical origin of the trend in the adsorption energies of simple species over ternary oxides is still an open question. In this contribution, BEEF-vdW+U calculations have been performed to calculate chemisorption energies of H, C, O, and CH_3 on the defect-free BO_2-terminated surface of a wide range of perovskites with various crystal structures. The reason these species are focused is that they are most frequently encountered adsorbed species in heterogeneous catalytic reactions. Then, in addition to surface O p-band center, the surface oxygen and metal vacancy formation energies are used to describe the trend in the chemisorption energies. Next, electronic structure analysis is carried out to explain the scaling relations established. Finally, we conclude by discussing the implication of our results for understanding the surface oxygen vacancy formation energy as a better descriptor that explains the trend in the chemisorption energies.

II COMPUTATIONAL METHODS

2.1 Selection of materials

The chemisorption energies on 81 perovskites have been calculated, in which A-site cations include alkali (K, Rb, and Cs), alkaline earth (Sr and Ba), and rare earth (La, Ce, Pr, Nd, Sm, Gd, Tb, Dy, and Ho) metals and B-site cations include d-block transition metals. The Goldschmidt tolerance factor (t_p)[29] of these perovskites is calculated to be in the range of 0.8 - 1.1 to ensure the stability of the crystal structure[30-31], which is defined as

$$t_p = \frac{r_A + r_O}{\sqrt{2}\left(r_B + r_O\right)} \quad (1)$$

where r_A, r_B, and r_O are the ionic radii of A-site cations, B-site cations, and O anions, respectively. The rare earth metals Pm and Eu are not taken into consideration because of the radioactivity and the limitation of the PAW potentials, respectively. Upon geometry optimization, all crystal structures can be classified into perfect cubic lattice (without tilting and Jahn-Teller distortions of BO_6 octahedra), rhombohedral lattice (with tilting of BO_6 octahedra), and orthorhombic lattice (with both tilting and Jahn-Teller distortions of BO_6 octahedra). The summary of the crystal structure of perovskites is given in TABLE S1 in the Supporting Information. The calculated crystal structures are predicted to be the same as those measured in experiment (see TABLE S2) and the relative error in the calculated lattice volume is less than 5%, as indicated in Figure S1. The BO_2-terminated surface, which was reported to be the most stable surface[32-33], was represented as a 5-layer slab with a p(1 × 1) cell, and a 12 Å vacuum spacing was applied to separate periodic slabs in the direction perpendicular to the perovskite surface. The surfaces that undergo significant reconstruction upon geometry optimization and adsorption of simple species are not taken into consideration.

Because the used 5-layer slab is symmetrical, as shown schematically in Figure 1, dipole correction was not applied in the direction perpendicular to the surface. On the other hand, since the highly symmetrical 5-layer slab employed is non-stoichiometric, compensating charge is usually required to achieve electrostatic stabilization of the charged atomic layers. Here the adsorption energies of H over a stoichiometric 6-layer slab were also calculated to ensure the convergence of

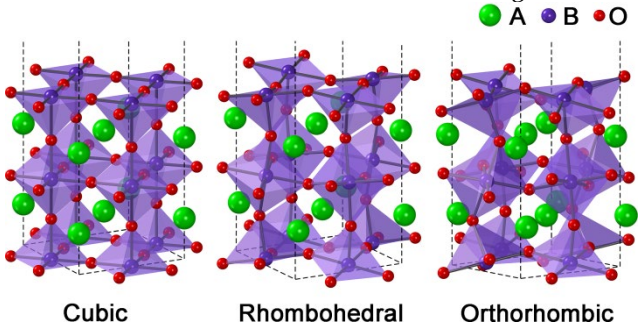

Figure 1. BO_2-terminated surface structures of perovskites with cubic, rhombohedral, and orthorhombic crystal structures.

adsorption energies with respect to slab thickness (see Table S3), and the tabulated values indicate that the differences between the chemisorption energies of H at the O site and B site are less than 0.13 eV and 0.07 eV, respectively, which fall well within the inherent uncertainty of DFT calculations.

The oxygen- or metal-deficient surface is constructed by removing one surface oxygen or metal atom from the defect-free BO_2-terminated surface, respectively. H and CH_3 are adsorbed on top of the O and B sites while C and O are positioned at the B site of the defect-free surfaces. Figure 1 shows that the exposed B-site cations on the BO_2-terminated surface of all the perovskites and the O anions on the surface of the cubic perovskites are equivalent. By contrast, the exposed O anions on the surfaces of rhombohedral and orthorhombic perovskites are divided into two groups, which lie above and below the B-site cations. The most stable oxygen-deficient surfaces and adsorption configurations of the simple species at the O site are shown in Figure S2.

2.2 DFT calculation

All self-consistent DFT calculations were carried out with the Vienna Ab-initio Simulation Package (VASP) software package[34]. The wavefunction at each k-point is calculated with a plane wave basis set. The projector-augmented wave (PAW) method was applied to represent the interactions between ion cores and valence electrons[35] and the Bayesian error estimation functional with van der Waals correlation (BEEF-vdW)[36] was used to account for the exchange and correlation of the Kohn-Sham theory, with an effective interaction parameter U_{eff} [37] addressing the on-site Coulomb interactions between the strongly correlated 3d electrons of the transition metal (see TABLE S4 for the U_{eff} values). By using the BEEF-vdW+U method with the same U_{eff} values, Zheng et al. [38] calculated the oxygen vacancy formation energies in $LaMO_3$ (M = Sc – Cu), which were found to be in remarkably good agreement with available experimental data, even better than was obtained from the HSE06 hybrid functional. We used the "hard" PAW potentials with valence configurations for all the elements listed in TABLE S5 and a plane-wave energy cutoff of up to 600 eV to converge the total energy per atom to within 1 meV. Moreover, sampling of the Brillouin zone was carried out with the Monkhorst-Pack method[39] and electronic occupancies were determined according to the Gaussian method with an energy smearing of 0.1 eV. A gamma-centered $7 \times 7 \times 5$ and $4 \times 4 \times 1$ k-point grid were used to sample the Brillouin zone of the crystal and surface structures of perovskites, respectively. For the majority of this work, spin-polarized calculations were performed to obtain reasonably accurate structures and energetics of perovskites unless magnetism is found to have no effect. The crystal structures of perovskites are optimized by using a conjugate-gradient algorithm and both the atomic coordinates and lattice vectors are allowed to relax until the forces on each atom are converged better than 0.01 eV/Å. During geometry optimization of the surface structures of perovskites, the bottom two layers of the slab were fixed at their crystal lattice positions while the adsorbate and the remainder of the slab were allowed to fully relax and the calculations are considered to be converged when the forces are less than 0.03 eV/Å.

III RESULTS AND DISCUSSION

3.1 Trend in chemisorption energies of simple species at the O site

3.1.1 Surface O p-band center

Our analysis begins with the linear scaling relations between the chemisorption energies of H and CH_3 at the O site and the surface O p-band center, which has been reported to be related to the redox capability of lattice oxygen of perovskites[40-41]. The chemisorption energy is calculated as

$$\Delta E_{ads,adsorbate} = E_{surface+adsorbate} - E_{surface} - E_{adsorbate} \quad (2)$$

where $E_{surface+adsorbate}$, $E_{surface}$, and $E_{adsorbate}$ are the calculated total energies of the surface with a species adsorbed, the defect-free surface, and a free adsorbate molecule, respectively.

As can be seen in Figure 2, the chemisorption energies of H and CH_3 at the O site scale with surface O p-band center over most perovskites. The reason surface O p-band center is correlated to the chemisorption energies is that it is intimately related to the adsorbate-oxygen bond strength. When the surface O p-band center becomes more negative, the downward shift of the p-band causes anti-bonding orbitals above the Fermi level to shift below it and become occupied by electrons. The increase in the occupation of anti-bonding orbitals leads to a weaker adsorbate-oxygen bond and a less negative chemisorption energy of simple species at the O site.

On the other hand, this linear correlation does not hold on two types of perovskites. One is $(Sr,Ba)BO_3$ (B = Ti, Zr, and Hf) and $LaRuO_3$ that are inert closed-shell compounds whose A- or B-site cations fulfill the 18-electron rule[25]. Because the electron configuration of the O anions in these perovskites is thermodynamically very stable, adsorbates can hardly form bands with oxygen, leading to a moderately negative chemisorption energy. The other type consists of $ARuO_3$ (A = Ce - Ho). The surface O p-band center does not change very much with the A-site cation and varies in a range of only 0.05 eV as A-site cations change from Ce to Ho. Clearly, such narrowly distributed surface O p-band centers are not capable of describing the trend in the chemisorption energies, as shown in Figure 2(c) and 2(f).

3.1.2 Surface oxygen vacancy formation energy

As surface O p-band center cannot describe the trend in the chemisorption energies on $ARuO_3$ (A = La – Ho),

surface oxygen vacancy formation energy ($\Delta E_{f,O\text{-}vac}$), a quantity of crucial importance for determining the

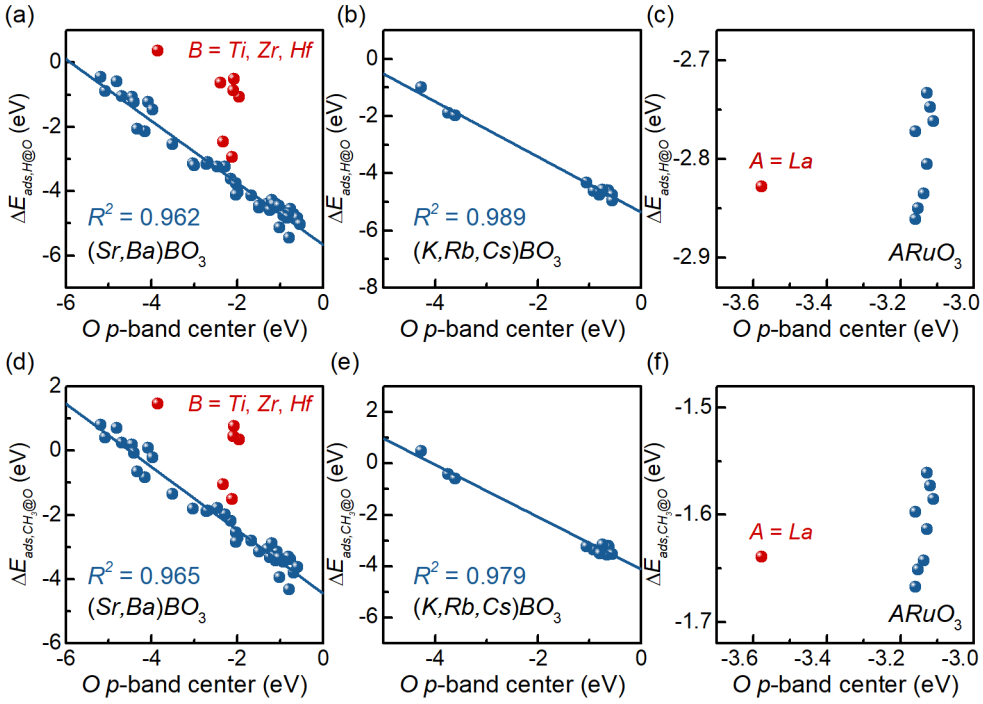

Figure 2. Scaling relations between surface O p-band center and $\Delta E_{ads,H@O}$ on (a) (Sr,Ba)BO_3, (b) (K,Rb,Cs)BO_3, and (c) $ARuO_3$; scaling relations between surface O p-band center and $\Delta E_{ads,CH_3@O}$ on (d) (Sr,Ba)BO_3, (e) (K,Rb,Cs)BO_3, and (f) $ARuO_3$.

catalytic activity in redox catalysis[42], is correlated to the chemisorption energies. The $\Delta E_{f,O\text{-}vac}$ is calculated as

$$\Delta E_{f,O\text{-}vac} = E_{surface}^{O-deficient} + \frac{1}{2}E_{O_2(g),corrected} - E_{surface} \quad (3)$$

where $E_{surface}^{O-deficient}$ is the total energy of the surface with an oxygen atom removed, and $E_{O_2(g),corrected}$ denotes the total energy of an isolated O_2 molecule with the binding energy corrected, which is due to the fact that the GGA method always overestimates the binding energy of oxygen[37, 43].

To understand better the relationship between $\Delta E_{f,O\text{-}vac}$ and $\Delta E_{ads,adsorbate@O}$, it is useful to decompose $\Delta E_{ads,adsorbate@O}$ into three contributions. The decomposition of $\Delta E_{ads,H@O}$ is shown in Eq. (4).

$$\begin{aligned}\Delta E_{ads,H@O} &= E_{surface+H} - E_{surface} - \frac{1}{2}E_{H_2(g)} \\ &= E_{surface+H} - E_{surface}^{O-deficient} - E_{OH(g)} \\ &+ E_{surface}^{O-deficient} + \frac{1}{2}E_{O_2(g),corrected} - E_{surface} \\ &+ E_{OH(g)} - \frac{1}{2}E_{O_2(g),corrected} - \frac{1}{2}E_{H_2(g)} \\ &= \Delta E_{ads,OH@O\text{-}vac}^{O-deficient} + \Delta E_{f,O\text{-}vac} + \Delta E_{f,OH(g)}\end{aligned} \quad (4)$$

where $\Delta E_{ads,OH@O\text{-}vac}^{O-deficient}$ is the chemisorption energy of OH(g) in the oxygen vacancy on the oxygen-deficient surface,

$$\begin{aligned}\Delta E_{ads,OH@O\text{-}vac}^{O-deficient} &= E_{surface+OH}^{O-deficient} - E_{surface}^{O-deficient} - E_{OH(g)} \\ &= E_{surface+H} - E_{surface}^{O-deficient} - E_{OH(g)}\end{aligned} \quad (5)$$

and $\Delta E_{f,OH(g)}$ is the formation energy of gaseous OH,

$$\Delta E_{f,OH(g)} = E_{OH(g)} - \frac{1}{2}E_{H_2(g)} - \frac{1}{2}E_{O_2(g),corrected} \quad (6)$$

As indicated in Figure 3(a-h), $\Delta E_{ads,OH@O\text{-}vac}^{O-deficient}$ scales linearly with $\Delta E_{f,O\text{-}vac}$ and, consequently, $\Delta E_{ads,H@O}$ can be expressed in terms of $\Delta E_{f,O\text{-}vac}$. The differences in the slope and intercept between the $\Delta E_{ads,H@O}$ and $\Delta E_{ads,OH@O\text{-}vac}^{O-deficient}$ plots are unity and $\Delta E_{f,OH(g)}$, respectively. The reasoning behind these scaling relations is that the formation of surface oxygen vacancy is the reverse of the adsorption of O in the oxygen vacancy and the adsorption configuration of OH in the oxygen vacancy resembles that of O at the same site. Because the scaling relation between the chemisorption energies of similar species at the same site is determined primarily by the chemical properties of adsorbates, it can be deduced that the choice of oxide surfaces has a negligible effect on the slope of the scaling relations. When OH or O adsorbs in the oxygen vacancy, two B-O bonds are formed, and the bond strength scales with the electron density of the adsorbate, as reported by Abild-Pedersen et al.[19]. As the oxygen atom of OH gains one electron from H, the number of valence electrons of O in OH is only half of

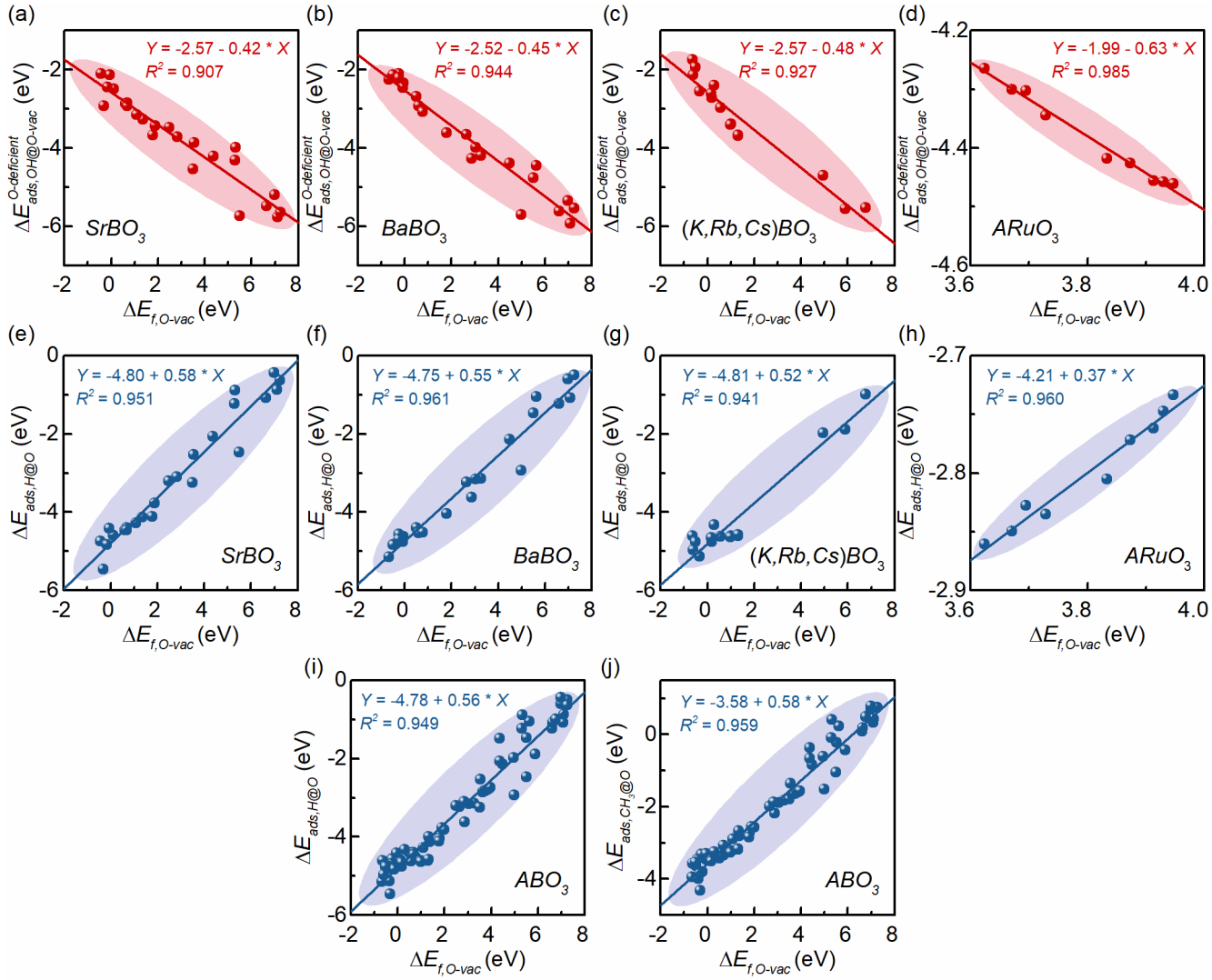

Figure 3. Scaling relations between $\Delta E_{f,O\text{-}vac}$ and $\Delta E^{O-deficient}_{ads,OH@O\text{-}vac}$ on (a) $SrBO_3$, (b) $BaBO_3$, (c) $(K,Rb,Cs)BO_3$, and (d) $ARuO_3$; scaling relations between $\Delta E_{f,O\text{-}vac}$ and $\Delta E_{ads,H@O}$ on (e) $SrBO_3$, (f) $BaBO_3$, (g) $(K,Rb,Cs)BO_3$, and (h) $ARuO_3$; (i) scaling relation between $\Delta E_{f,O\text{-}vac}$ and $\Delta E_{ads,H@O}$ over all the perovskites under consideration; (j) scaling relation between $\Delta E_{f,O\text{-}vac}$ and $\Delta E_{ads,CH_3@O}$ over all the perovskites under consideration.

that of O, indicating that H donates half of the electrons needed by the O atom and causes the slope of the plot $\Delta E^{O-deficient}_{ads,OH@O\text{-}vac}$ vs. $\Delta E_{f,O\text{-}vac}$ to be nearly -0.5.

Indeed, the differences in the slope and intercept of the $\Delta E^{O-deficient}_{ads,OH@O\text{-}vac}$ versus $\Delta E_{f,O\text{-}vac}$ plots over different perovskites are less than 0.1 except for $ARuO_3$. This phenomenon can be explained by the much narrower range of the adsorption energies on $ARuO_3$ than on the other perovskites, making it more sensitive to the inherent error caused by the DFT method. Consequently, the scaling relation between $\Delta E_{f,O\text{-}vac}$ and $\Delta E_{ads,H@O}$ on all the perovskite surfaces under consideration can be established, as shown in Figure 3(i). The similar relationship between $\Delta E_{ads,OH}$ and $\Delta E_{ads,O}$ on the defect-free surfaces of transition metals and binary oxides has been reported by Calle-Vallejo et al.[25], and the slope that is close to 0.5 was believed to arise from the difference in the number of valence electrons of O. Hence, it can be concluded that this scaling relation holds true regardless of the surface of interest. Like $\Delta E_{ads,H@O}$, $\Delta E_{ads,CH_3@O}$ also scales linearly with $\Delta E_{f,O\text{-}vac}$, as shown in Figure 3(j). The slopes of these two fitted straight lines are almost the same because both H and CH_3 donate one unpaired electron to form a σ bond with oxygen, resulting in similar electron densities around the oxygen atom of OH and OCH_3.

In addition, the scaling relations between $\Delta E_{ads,H@O}$, $\Delta E_{ads,CH_3@O}$ and $\Delta E_{f,O\text{-}vac}$ on $BaBO_3$ are calculated by the PBE+U method, as shown in Figure S3. It is found that the differences in the slope and intercept of the scaling relations between BEEF-vdW+U and PBE+U are only 0.01 and 0.04 eV, respectively, indicating that the exchange-

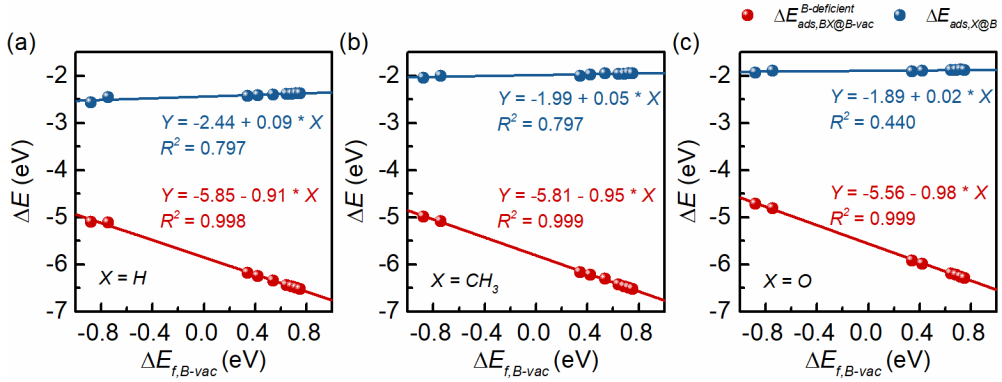

Figure 4. Scaling relations between $\Delta E_{f,B\text{-vac}}$ and (a) $\Delta E^{B-deficient}_{ads,BH@B\text{-vac}}$ and $\Delta E_{ads,H@B}$, (b) $\Delta E^{B-deficient}_{ads,BCH_3@B\text{-vac}}$ and $\Delta E_{ads,CH_3@B}$, and (c) $\Delta E^{B-deficient}_{ads,BO@B\text{-vac}}$ and $\Delta E_{ads,O@B}$ on $ARuO_3$.

correlation functional used also has a negligible effect on the chemisorption energy scaling relations on perovskites.

Compared with surface O p-band center, the change in $\Delta E_{f,O\text{-vac}}$ determines the trend in the chemisorption energies on perovskites because $\Delta E_{f,O\text{-vac}}$ is more sensitive to the change in the electron structure of perovskites. As shown in Figures 3(h), the $\Delta E_{f,O\text{-vac}}$ on $ARuO_3$ is distributed over a much broader range (0.33 eV) than the surface O p-band center and therefore scales linearly with the chemisorption energies of the simple species at the O site.

3.2 Trend in chemisorption energies of simple species at the B site

3.2.1 Surface metal vacancy formation energy

Inspired by the success of $\Delta E_{f,O\text{-vac}}$ as a good descriptor of the trend in the chemisorption energies at the O site, attempts have been made to correlate the surface metal vacancy formation energy ($\Delta E_{f,B\text{-vac}}$) to the chemisorption energies at the B site on perovskites, as there is no comprehensive theoretical work that has been devoted to understanding the adsorption behavior of C-containing species at the B site on perovskite surfaces. Likewise, $\Delta E_{f,B\text{-vac}}$ is calculated as

$$\Delta E_{f,B\text{-vac}} = E^{B-deficient}_{surface} + E_B - \Delta E_B - E_{surface} \quad (7)$$

where $E^{B-deficient}_{surface}$ is the calculated total energy of the surface with a B-site metal vacancy, E_B is the total energy per atom in bulk metal, and ΔE_B is the energy correction to the total energies calculated by BEEF-vdW+U, which makes it possible to directly compare $E^{B-deficient}_{surface}$ and $E_{surface}$ that are obtained by BEEF-vdW+U and E_B that is obtained by the BEEF-vdW method. The chemisorption energies of species at the B site can also be decomposed into three contributions in a similar way in which the chemisorption energies of species at the O site are decomposed. The $\Delta E_{ads,H@B}$ can be decomposed as

$$\Delta E_{ads,H@B} = \Delta E^{B-deficient}_{ads,BH@B\text{-vac}} + \Delta E_{f,B\text{-vac}} + \Delta E_{f,BH(g)} \quad (8)$$

For $ARuO_3$ where the B-site cations remain the same, the plot of the $\Delta E_{ads,H@B}$ against the $\Delta E_{f,B\text{-vac}}$ yields a straight line because the $\Delta E^{B-deficient}_{ads,BH@B\text{-vac}}$ scales linearly with $\Delta E_{f,B\text{-vac}}$. As shown in Figure 4(a), the slope of the scaling relation between $\Delta E_{f,B\text{-vac}}$ and $\Delta E^{B-deficient}_{ads,BH@B\text{-vac}}$ is also determined by the electron density of the atom bound to the surface. According to the Bader charge analysis, the effective Bader charge on Ru changes by ~1.36 $|e|$ and ~1.20 $|e|$ upon chemisorption of Ru and RuH in the metal vacancy on the defective surface, respectively; that is, about ~88 % of the electron density needed by the Ru atom of RuH is donated by surface O anions. Interestingly, this value is rather close to the slope of the $\Delta E^{B-deficient}_{ads,BH@B\text{-vac}}$ versus $\Delta E_{f,B\text{-vac}}$ plot (0.91). Similarly, the variation of the chemisorption energies of CH_3 and O can also be described by $\Delta E_{f,B\text{-vac}}$, as shown in Figure 4(b-c). $\Delta E_{ads,C@B}$ does not correlate to $\Delta E_{f,B\text{-vac}}$ because the oxide surfaces are reconstructed to different extents when C is bonded to the B-site cation[44], which is reflected in the variation in the B-O bond length from ~2.0 Å to ~2.4 Å.

As for $(K,Rb,Cs,Sr,Ba)BO_3$, the relation between $\Delta E_{f,B\text{-vac}}$ and the chemisorption energies of the simple species at the B site is more sophisticated because the atom to which the adsorbates are bound varies with perovskite. The change in the electron density around the B-site cations upon formation of metal hydride depends strongly on the electron affinity of the B-site cations and, consequently, plotting the $\Delta E^{B-deficient}_{ads,BH@B\text{-vac}}$ against $\Delta E_{f,B\text{-vac}}$ does not give a straight line. Furthermore, the formation energy of metal hydride $\Delta E_{f,BH(g)}$ also varies with the B-site cation and is no longer a constant. As a consequence, the $\Delta E_{f,B\text{-vac}}$ is not a suitable descriptor to explain the trend in the chemisorption energies of the simple species at the B site on $(K,Rb,Cs,Sr,Ba)BO_3$.

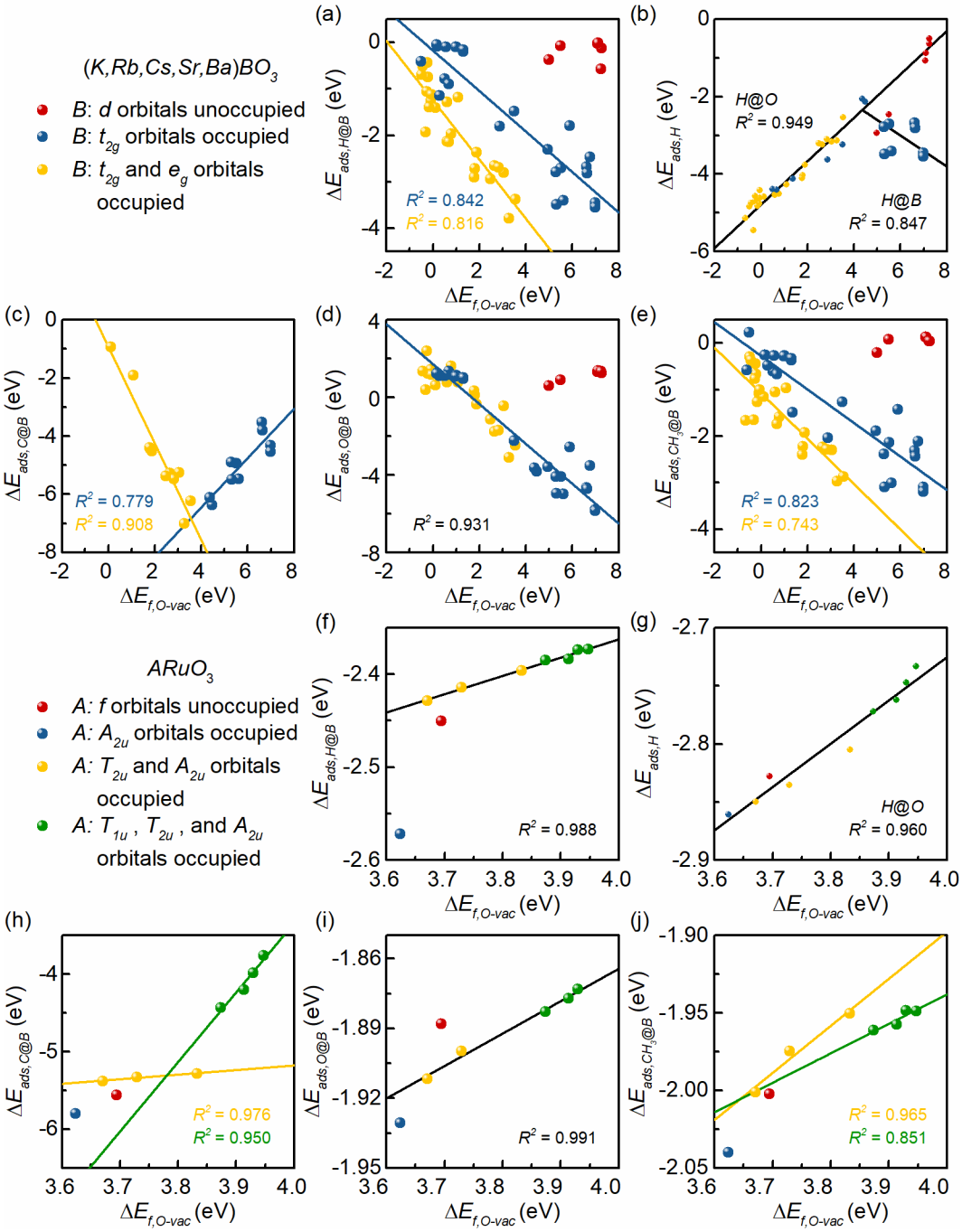

Figure 5. Scaling relations between $\Delta E_{f,O\text{-}vac}$ and (a) $\Delta E_{ads,H@B}$, (b) $\Delta E_{ads,H}$, (c) $\Delta E_{ads,C@B}$, (d) $\Delta E_{ads,O@B}$, (e) $\Delta E_{ads,CH_3@B}$ on (K,Rb,Cs,Sr,Ba)BO_3; scaling relations between $\Delta E_{f,O\text{-}vac}$ and (f) $\Delta E_{ads,H@B}$, (g) $\Delta E_{ads,H}$, (h) $\Delta E_{ads,C@B}$, (i) $\Delta E_{ads,O@B}$, (j) $\Delta E_{ads,CH_3@B}$ on $ARuO_3$. The small and large spheres in Figure 5(b) and 5(g) indicate the $\Delta E_{ads,H@O}$ on (K,Rb,Cs,Sr,Ba)BO_3 and $ARuO_3$ and $\Delta E_{ads,H@B}$ on (K,Rb,Cs,Sr,Ba)BO_3, respectively.

3.2.2 Surface oxygen vacancy formation energy

Because of the failure of the $\Delta E_{f,B\text{-}vac}$ in describing the trend in the chemisorption energies of the simple species at the B site on (K,Rb,Cs,Sr,Ba)BO_3, the $\Delta E_{f,O\text{-}vac}$ is correlated to the chemisorption energies to see whether the $\Delta E_{f,O\text{-}vac}$ can be used as a reasonable descriptor. As shown in Figure 5(a-e), the chemisorption energies of H, C, O, and CH_3 scale linearly with the $\Delta E_{f,O\text{-}vac}$, depending on the splitting and filling of d orbitals, as illustrated in Figure 6(a). In this way, (K,Rb,Cs,Sr,Ba)BO_3 can be classified into three categories. The first group consists of (K,Rb,Cs,Sr,Ba)BO_3 perovskites containing B-site cations with d orbitals unoccupied, and the stable electron configuration makes it hard to gain or lose electrons. The second group contains (K,Rb,Cs,Sr,Ba)BO_3 with B-site cations having only the t_{2g} set occupied. The last group consists of perovskites having transition-metal cations with both the t_{2g} and e_g sets occupied.

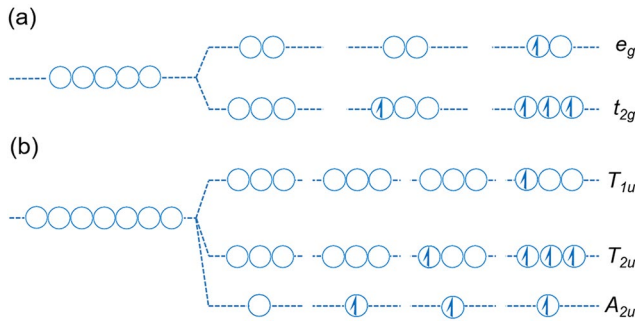

Figure 6. Illustrations of (a) splitting of d orbitals and occupation of t_{2g} and e_g orbitals on the B-site cation on $(K,Rb,Cs,Sr,Ba)BO_3$ and (b) splitting of f orbitals and occupation of A_{2u}, T_{2u}, and T_{1u} orbitals on the A-site cation on $ARuO_3$.

The chemisorption energies on the first type of perovskites are close to zero because the B-site cations have a stable electron configuration and can hardly form a chemical bond with adsorbates. As for the chemisorption energies on the latter two types of perovskites, there mostly exists a great discrepancy between the fitted straights lines because of the difference in the nature of the bonding between the B-site cation and the adsorbate. Upon adsorption at the B site, H forms a metal(t_{2g})-H(s) σ bond with the B-site cation when only the t_{2g} set is occupied, while a metal(e_g)-H(s) σ bond will be formed when the B-site cation has both the t_{2g} and the e_g sets occupied. In the metal(e_g)-H(s) σ bond, the electron density lies directly along the bond axis. By comparison, the t_{2g} orbitals have lobes that are directed between the bond axis and overlap with the H s orbital in a somewhat sideways fashion, thereby giving rise to σ bonds that have fewer contributions from d electrons. As a consequence, the adsorption heat of H on the surface of the second and third types of perovskites varies with the $\Delta E_{f,O\text{-}vac}$ in different ways. Similarly, CH_3 also has an unpaired electron to from a σ bond with the B-site cation and a similar trend in $\Delta E_{ads,CH_3@B}$ is observed.

In addition, the most negative $\Delta E_{ads,H}$ for each perovskite are obtained by comparing the $\Delta E_{ads,H@O}$ and $\Delta E_{ads,H@B}$, which is then plotted against the $\Delta E_{f,O\text{-}vac}$, as shown in Figure 5(b). From the figure, one can see that, as the $\Delta E_{f,O\text{-}vac}$ increases, $\Delta E_{ads,H@O}$ becomes less negative and $\Delta E_{ads,H@B}$ changes in the opposite way. Moreover, when $\Delta E_{f,O\text{-}vac}$ is greater than 4 eV, H tends to be adsorbed at the B site on the surface of the second type of perovskites and $\Delta E_{ads,H}$ turns to be inversely proportional to $\Delta E_{f,O\text{-}vac}$.

Figure 5(c) shows that the $\Delta E_{ads,C@B}$ on $(K,Rb,Cs,Sr,Ba)BO_3$ scales linearly with $\Delta E_{f,O\text{-}vac}$. It is important to note that some $\Delta E_{ads,C@B}$ values are removed from the figure because on these surfaces adsorption of C would lead to significant surface reconstruction to different degrees, which makes the trend obtained deviate greatly from it should be. The slope of the $\Delta E_{ads,C@B}$ vs. $\Delta E_{f,O\text{-}vac}$ plot on the second type of perovskites is positive while that on the third type of perovskites is negative. The similar trend has been observed when studying the metal–carbon adhesion energies[45] and the bond dissociation energies of carbides of early and late transition metals[46]. The reason can be traced to the fact that the trend in $\Delta E_{ads,C@B}$ on the second type of perovskites whose B-site cations are mostly early transition metal cations, is determined largely by the order of the metal(t_{2g})-C(p) π bonds[47]. The greater the number of electrons about the metal cation, the greater the number of electrons that would be shared with the C atom, and hence the stronger is the B-C bond. As for the third type of perovskites, the trend in $\Delta E_{ads,C@B}$ is related to the ionic bond order of the metal(e_g)-C(p) σ bond because the metal(e_g)-C(p) σ bond is characterized as ionic with less covalent character than the metal(t_{2g})-C(p) π bonds. Hence, the B-C bond strength is determined predominantly by electrostatic interactions between the metal and the carbon ions. As the electron affinity of B-site cations increases, C withdraws fewer electrons from the B-site cation and the $\Delta E_{ads,C@B}$ becomes less negative. As a consequence, the $\Delta E_{ads,C@B}$ on the second and third type of perovskites follows the different trends.

As for the $\Delta E_{ads,O@B}$, it can be found that the same scaling relation holds on both the second and the third types of perovskites. The reasoning behind this fact is that upon formation of an oxygen vacancy the B-O bonds are broken while the adsorption of O at the B site is a reverse process of the formation of a B-O bond. That is to say, the $\Delta E_{f,O\text{-}vac}$ and $\Delta E_{ads,O@B}$ are both determined by the B-O bond strength, regardless of whether σ or π bonds are formed, which results in the slope of the linear scaling relation between $\Delta E_{f,O\text{-}vac}$ and $\Delta E_{ads,O@B}$ close to -1.

The scaling relations between the chemisorption energies of H, C, O, and CH_3 on $ARuO_3$ and $\Delta E_{f,O\text{-}vac}$ are illustrated in Figure 5(f-j). By analogy to the classification of $(K,Rb,Cs,Sr,Ba)BO_3$, $ARuO_3$ can also be classified into four categories according to the electron configuration of the A-site cations, as illustrated in Figure 6(b). The first type of $ARuO_3$ is the ones where A-site cations have the stable noble-gas electron configuration. The second type has the A-site cations with 4f electron in the occupied A_{2u} orbital under the influence of the crystal field[48]. As the atomic number increases, the A-site cations in the third type have 4f electrons filling the triply degenerate T_{2u} and A_{2u} orbitals, and the A-site cations in the fourth type of perovskites have more 4f electrons filling the T_{1u} orbitals besides T_{2u} and A_{2u} orbitals. By using the Bader charge analysis (see Figure S4), it is found that electron configuration of the A-site cations not only plays a role in determining the charge they carry but also has a dramatic effect on the charges carried by the B-site cations and O anions. Within each type of perovskites, as the effective Bader charge on the Ru cations becomes more positive, the decreased electron density reduces their ability to

donate electrons, which leads to less negative chemisorption energies at the Ru site.

As indicated in Figures 3 and 5, the $\Delta E_{f,O\text{-}vac}$ can be used to explain the trend in the chemisorption energies of the simple species at both the O and the B sites when perovskites are classified into several categories on the basis of the electron configuration of the B- or A-site cations. Compared with the $\Delta E_{f,B\text{-}vac}$ which scales with the chemisorption energy of the simple species at the B site only if the B-site cations remain the same, the $\Delta E_{f,O\text{-}vac}$ is a much more general descriptor that can be used to describe the adsorption behaviors of almost all the perovskites.

3.3 Origin of chemisorption energy scaling relations

To further investigate the origin of the linear scaling relations between surface oxygen vacancy formation energies and the chemisorption energies, the actual partial charge on the O anions and B-site cations is calculated to provide a rational interpretation of the chemisorption energy scaling relations. Previously, Su et al. examined the scaling relations between the chemisorption energies of ionically and covalently bound species by correlating the adsorption energies on transition metals to the excess Bader charge on the adsorbates[49]. As indicated in Figure 7, the $\Delta E_{f,O\text{-}vac}$ depends strongly upon the effective Bader charge on the O anions (q_O) and B-site cations (q_B), which therefore plays a significant role in determining the adsorption activity of the ions.

According to the decomposition of $\Delta E_{f,O\text{-}vac}$ proposed by Zheng et al.[38], the change in the $\Delta E_{f,O\text{-}vac}$ is determined by the variation of the bonding energy ($\Delta E_{bonding}$), the energy required to remove an oxygen atom from the surface. $\Delta E_{bonding}$ can be further divided into the change in the electronic potential energy ($\Delta E_{electrostatic}$) and the energy associated with the charge transfer from the O anion to the remaining surface ($\Delta E_{transfer}$), both of which are closely related to the effective Bader charge on the O anions. As the effective Bader charge on the O anions becomes less negative, the O anions interact more weakly with the cations in the tightly bonded solids, leading to a less positive $\Delta E_{electrostatic}$. On the other hand, the $\Delta E_{transfer}$ takes less negative values as less amounts of electrons left behind upon oxygen removal are transferred to the remaining oxide lattice. Because the $\Delta E_{electrostatic}$ plays a more important role than $\Delta E_{transfer}$ [38] in determining $\Delta E_{bonding}$, the $\Delta E_{bonding}$ becomes less positive and so does $\Delta E_{f,O\text{-}vac}$. In addition, as the q_O becomes less negative, the decreased electron density around the O anion would enhance its ability to withdraw electrons from the adsorbate[50], which leads to a more negative chemisorption energy. Hence, the q_O explains the trend

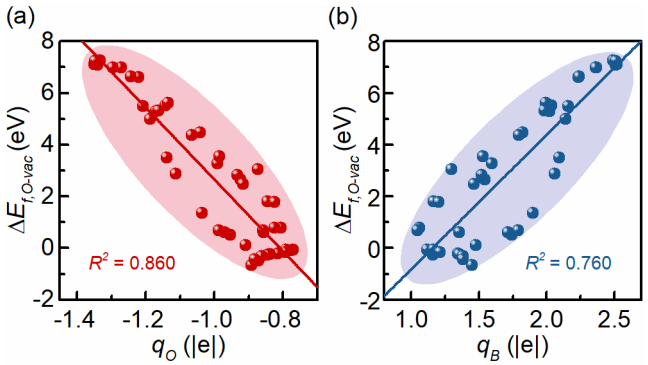

Figure 7. Scaling relations between $\Delta E_{f,O\text{-}vac}$ and (a) the effective Bader charge on the O anion and (b) the effective Bader charge on the B-site cation on $(Sr,Ba)BO_3$.

in the chemisorption energies of simple species at the O site.

From Figure 7(b), it is found that the variation of the $\Delta E_{f,O\text{-}vac}$ can also be described by the effective Bader charge on the B-site cations. The B-site cation that donates more electrons to the lattice oxygen can also donate more electrons to the adsorbate bound onto it. The strength of the metal-adsorbate interaction would be determined by q_B and how the d orbitals are occupied. Hence, the actual partial charge on either the O anion or the B-site cation explains the electronic origin of the chemisorption energy scaling relations over perovskites.

IV SUMMARY

In this work, BEEF-vdW+U calculations have been carried out to shed light on the dependence of the chemisorption energies of H, C, O, and CH_3 on the defect-free BO_2-terminated surfaces of a wide range of perovskites on the electronic structures of the perovskite surfaces. Our calculated results indicate that the previously proposed surface O p-band center can be used to describe the trend in the chemisorption energies at the O site of perovskites except $(Sr,Ba)BO_3$ (B = Ti, Zr, Hf) and $ARuO_3$ (A = La - Ho). By comparison, the change in the surface oxygen vacancy formation energy largely determines the variation in the chemisorption energy on all the perovskites under consideration because the surface oxygen vacancy formation energy is more sensitive to the change in the electron structure of perovskites.

As for the chemisorption energies at the B site, on the one hand, the surface metal vacancy formation energy is a reasonable descriptor of the trend in the chemisorption energies on the $ARuO_3$ (A = La - Ho) perovskites that have the same B-site cation. On the other hand, according to the splitting and filling of the d- and f-orbitals of the B- and A-site cations, respectively, the perovskites could be classified into several categories. In each category, the chemisorption energies at the B site on $(K,Rb,Cs,Sr,Ba)BO_3$ (B = d-block transition metals) and $ARuO_3$ are closely related to the strength of the ionic bonding in the perovskites.

The surface oxygen vacancy formation energy can be used as a descriptor to explain the trend in the calculated adsorption energies at either the O or the B site. The scaling relations established can be traced to the fact that the surface oxygen vacancy formation energy is closely related to the actual partial charge on the oxygen and transition metal ions. The larger the actual partial charges the oxygen and transition metal ions carry, the stronger the B-O bond, which in turn gives rise to a weakened and an enhanced ability of the O anions to withdraw and of the B cations to donate electrons to the adsorbates, respectively.

ASSOCIATED CONTENT

Supporting Information.

The crystal structure of perovskites; experimental lattice volumes and relative error of calculated lattice volume of perovskites; adsorption structures of H, CH_3, C, and O on the perovskite(001) surfaces; U_{eff} and ΔE_M values and PAW potentials for metals and oxygen; scaling relations between $\Delta E_{f,O\text{-}vac}$ and chemisorption energies of H and CH_3 calculated by PBE+U; scaling relations between atomic number of A-site cations and the effective Bader charge on A-, B-site cations and O anions of $ARuO_3$ (A = La - Ho); and the binding energies and Cartesian coordinates of some representative surfaces can be found in the Supporting Information.

This material is available free of charge via the Internet at http://pubs.acs.org.

AUTHOR INFORMATION

Corresponding Author

*E-mail: yanzhu@ecust.edu.cn

ORCID

Zhi-Jun Sui: 0000-0002-7819-6205
De Chen: 0000-0002-5609-5825
Yi-An Zhu: 0000-0001-6226-0711

Notes

The authors declare no competing financial interest.

ACKNOWLEDGMENT

This work is supported by the Natural Science Foundation of China (21473053, 91645122, and U1663221), the National Key Research and Development Program of China (2018YFB0604700), and the Fundamental Research Funds for the Central Universities (222201718003). The computational time provided by the Notur project is highly acknowledged.

REFERENCES

(1) Adler, S. B., Factors Governing Oxygen Reduction in Solid Oxide Fuel Cell Cathodes. *Chem. Rev.* **2004**, *104*, 4791-4844.

(2) Fergus, J. W., Perovskite Oxides for Semiconductor-Based Gas Sensors. *Sens. Actuators, B* **2007**, *123*, 1169-1179.

(3) Gupta, S.; Mahapatra, M. K.; Singh, P., Lanthanum Chromite Based Perovskites for Oxygen Transport Membrane. *Mater. Sci. Eng., R* **2015**, *90*, 1-36.

(4) Royer, S.; Duprez, D.; Can, F.; Courtois, X.; Batiot-Dupeyrat, C.; Laassiri, S.; Alamdari, H., Perovskites as Substitutes of Noble Metals for Heterogeneous Catalysis: Dream or Reality. *Chem. Rev.* **2014**, *114*, 10292-10368.

(5) Zhu, H.; Zhang, P.; Dai, S., Recent Advances of Lanthanum-Based Perovskite Oxides for Catalysis. *ACS Catal.* **2015**, *5*, 6370-6385.

(6) Aliotta, C.; Liotta, L. F.; Deganello, F.; La Parola, V.; Martorana, A., Direct Methane Oxidation on $La_{1-x}Sr_xCr_{1-y}Fe_yO_{3-\delta}$ Perovskite-Type Oxides as Potential Anode for Intermediate Temperature Solid Oxide Fuel Cells. *Appl. Catal., B* **2016**, *180*, 424-433.

(7) Michalsky, R.; Neuhaus, D.; Steinfeld, A., Carbon Dioxide Reforming of Methane Using an Isothermal Redox Membrane Reactor. *Energy Technol.* **2015**, *3*, 784-789.

(8) Gangurde, L. S.; Sturm, G. S. J.; Valero-Romero, M. J.; Mallada, R.; Santamaria, J.; Stankiewicz, A. I.; Stefanidis, G. D., Synthesis, Characterization, and Application of Ruthenium-Doped $SrTiO_3$ Perovskite Catalysts for Microwave-Assisted Methane Dry Reforming. *Chem. Eng. Process.* **2018**, *127*, 178-190.

(9) Valderrama, G.; Kiennemann, A.; de Navarro, C. U.; Goldwasser, M. R., $LaNi_{1-x}Mn_xO_3$ Perovskite-Type Oxides as Catalysts Precursors for Dry Reforming of Methane. *Appl. Catal., A* **2018**, *565*, 26-33.

(10) Mihai, O.; Chen, D.; Holmen, A., Catalytic Consequence of Oxygen of Lanthanum Ferrite Perovskite in Chemical Looping Reforming of Methane. *Ind. Eng. Chem. Res.* **2011**, *50*, 2613-2621.

(11) Peña, M. A.; Fierro, J. L. G., Chemical Structures and Performance of Perovskite Oxides. *Chem. Rev.* **2001**, *101*, 1981-2018.

(12) Nørskov, J. K.; Studt, F.; Abild-Pedersen, F.; Bligaard, T., *Fundamental Concepts in Heterogeneous Catalysis*; John Wiley & Sons, 2014.

(13) Bronsted, J. N., Acid and Basic Catalysis. *Chem. Rev.* **1928**, *5*, 231-338.

(14) Evans, M.; Polanyi, M., Inertia and Driving Force of Chemical Reactions. *Trans. Faraday Soc.* **1938**, *34*, 11-24.

(15) Bligaard, T.; Nørskov, J. K.; Dahl, S.; Matthiesen, J.; Christensen, C. H.; Sehested, J., The Brønsted–Evans–Polanyi Relation and the Volcano Curve in Heterogeneous Catalysis. *J. Catal.* **2004**, *224*, 206-217.

(16) Nørskov, J. K.; Bligaard, T.; Logadottir, A.; Bahn, S.; Hansen, L. B.; Bollinger, M.; Bengaard, H.; Hammer, B.; Sljivancanin, Z.; Mavrikakis, M., Universality in Heterogeneous Catalysis. *J. Catal.* **2002**, *209*, 275-278.

(17) Latimer, A. A.; Kulkarni, A. R.; Aljama, H.; Montoya, J. H.; Yoo, J. S.; Tsai, C.; Abild-Pedersen, F.; Studt, F.; Nørskov, J. K., Understanding Trends in C–H Bond Activation in Heterogeneous Catalysis. *Nat. Mater.* **2017**, *16*, 225-229.

(18) Wang, C.-M.; Brogaard, R. Y.; Xie, Z.-K.; Studt, F., Transition-State Scaling Relations in Zeolite Catalysis: Influence of Framework Topology and Acid-Site Reactivity. *Catal. Sci. Technol.* **2015**, *5*, 2814-2820.

(19) Abild-Pedersen, F.; Greeley, J.; Studt, F.; Rossmeisl, J.; Munter, T. R.; Moses, P. G.; Skúlason, E.; Bligaard, T.; Nørskov, J. K., Scaling Properties of Adsorption Energies for Hydrogen-Containing Molecules on Transition-Metal Surfaces. *Phys. Rev. Lett.* **2007**, *99*, 016105.

(20) Montemore, M. M.; Medlin, J. W., Scaling Relations between Adsorption Energies for Computational Screening and Design of Catalysts. *Catal. Sci. Technol.* **2014**, *4*, 3748-3761.

(21) Calle-Vallejo, F.; Martínez, J. I.; García-Lastra, J. M.; Rossmeisl, J.; Koper, M. T. M., Physical and Chemical Nature of the Scaling Relations between Adsorption Energies of Atoms on Metal Surfaces. *Phys. Rev. Lett.* **2012**, *108*, 116103.

(22) Greeley, J., Theoretical Heterogeneous Catalysis: Scaling Relationships and Computational Catalyst Design. *Annu. Rev. Chem. Biomol. Eng.* **2016**, *7*, 605-635.
(23) Calle-Vallejo, F.; Loffreda, D.; Koper, M. T. M.; Sautet, P., Introducing Structural Sensitivity into Adsorption–Energy Scaling Relations by Means of Coordination Numbers. *Nat. Chem.* **2015**, *7*, 403-410.
(24) Montoya, J. H.; Doyle, A. D.; Nørskov, J. K.; Vojvodic, A., Trends in Adsorption of Electrocatalytic Water Splitting Intermediates on Cubic ABO_3 Oxides. *Phys. Chem. Chem. Phys.* **2018**, *20*, 3813-3818.
(25) Calle-Vallejo, F.; Inoglu, N. G.; Su, H.-Y.; Martínez, J. I.; Man, I. C.; Koper, M. T. M.; Kitchin, J. R.; Rossmeisl, J., Number of Outer Electrons as Descriptor for Adsorption Processes on Transition Metals and Their Oxides. *Chem. Sci.* **2013**, *4*, 1245-1249.
(26) Calle-Vallejo, F.; Díaz-Morales, O. A.; Kolb, M. J.; Koper, M. T. M., Why Is Bulk Thermochemistry a Good Descriptor for the Electrocatalytic Activity of Transition Metal Oxides? *ACS Catal.* **2015**, *5*, 869-873.
(27) Cohen, A. J.; Mori-Sánchez, P.; Yang, W., Insights into Current Limitations of Density Functional Theory. *Science* **2008**, *321*, 792-794.
(28) Lee, Y.-L.; Kleis, J.; Rossmeisl, J.; Morgan, D., Ab Initio Energetics of $LaBO_3$(001) (B = Mn, Fe, Co, and Ni) for Solid Oxide Fuel Cell Cathodes. *Phys. Rev. B* **2009**, *80*, 224101.
(29) Yokokawa, H., Understanding Materials Compatibility. *Ann. Rev. Mater. Res.* **2003**, *33*, 581-610.
(30) Filip, M. R.; Eperon, G. E.; Snaith, H. J.; Giustino, F., Steric Engineering of Metal-Halide Perovskites with Tunable Optical Band Gaps. *Nat. Commun.* **2014**, *5*, 5757.
(31) Uecker, R.; Wilke, H.; Schlom, D. G.; Velickov, B.; Reiche, P.; Polity, A.; Bernhagen, M.; Rossberg, M., Spiral Formation During Czochralski Growth of Rare-Earth Scandates. *J. Cryst. Growth* **2006**, *295*, 84-91.
(32) Choi, Y.; Mebane, D. S.; Lin, M. C.; Liu, M., Oxygen Reduction on $LaMnO_3$-Based Cathode Materials in Solid Oxide Fuel Cells. *Chem. Mater.* **2007**, *19*, 1690-1699.
(33) Evarestov, R. A.; Kotomin, E. A.; Mastrikov, Y. A.; Gryaznov, D.; Heifets, E.; Maier, J., Comparative Density-Functional LCAO and Plane-Wave Calculations of $LaMnO_3$ Surfaces. *Phys. Rev. B* **2005**, *72*, 214411.
(34) Kresse, G.; Furthmüller, J., Efficiency of Ab-Initio Total Energy Calculations for Metals and Semiconductors Using a Plane-Wave Basis Set. *Comp. Mater. Sci.* **1996**, *6*, 15-50.
(35) Blöchl, P. E., Projector Augmented-Wave Method. *Phys. Rev. B* **1994**, *50*, 17953-17979.
(36) Wellendorff, J.; Lundgaard, K. T.; Møgelhøj, A.; Petzold, V.; Landis, D. D.; Nørskov, J. K.; Bligaard, T.; Jacobsen, K. W., Density Functionals for Surface Science: Exchange-Correlation Model Development with Bayesian Error Estimation. *Phys. Rev. B* **2012**, *85*, 235149.
(37) Li, Y.; Zheng, Y.-S.; Zhu, Y.-A.; Sui, Z.-J.; Zhou, X.-G.; Chen, D.; Yuan, W.-K., BEEF-vdW+U Method Applied to Perovskites: Thermodynamic, Structural, Electronic, and Magnetic Properties. *J. Phys.: Condens. Matter* **2019**, *31*, 145901.
(38) Zheng, Y.-S.; Zhang, M.; Li, Q.; Zhu, Y.-A.; Sui, Z.-J.; Chen, D.; Zhou, X.-G., Electronic Origin of Oxygen Transport Behavior in La-Based Perovskites: A Density Functional Theory Study. *J. Phys. Chem. C* **2019**, *123*, 275-290.
(39) Monkhorst, H. J.; Pack, J. D., Special Points for Brillouin-Zone Integrations. *Phys. Rev. B* **1976**, *13*, 5188-5192.
(40) Hua, B.; Li, M.; Pang, W.; Tang, W.; Zhao, S.; Jin, Z.; Zeng, Y.; Shalchi Amirkhiz, B.; Luo, J.-L., Activating p-Blocking Centers in Perovskite for Efficient Water Splitting. *Chem* **2018**, *4*, 2902-2916.
(41) Grimaud, A.; May, K. J.; Carlton, C. E.; Lee, Y.-L.; Risch, M.; Hong, W. T.; Zhou, J.; Shao-Horn, Y., Double Perovskites as A Family of Highly Active Catalysts for Oxygen Evolution in Alkaline Solution. *Nat. Commun.* **2013**, *4*, 2439.
(42) Yang, J.; Zhang, J.; Liu, X.; Duan, X.; Wen, Y.; Chen, R.; Shan, B., Origin of the Superior Activity of Surface Doped $SmMn_2O_5$ Mullites for NO Oxidation: A First-Principles Based Microkinetic Study. *J. Catal.* **2018**, *359*, 122-129.
(43) Wang, L.; Maxisch, T.; Ceder, G., Oxidation Energies of Transition Metal Oxides within the GGA+U Framework. *Phys. Rev. B* **2006**, *73*, 195107.
(44) Van Santen Rutger, A., *Theoretical Heterogeneous Catalysis*; World Scientific, 1991.
(45) Silvearv, F.; Larsson, P.; Jones, S. L. T.; Ahuja, R.; Larsson, J. A., Establishing the Most Favorable Metal–Carbon Bond Strength for Carbon Nanotube Catalysts. *J. Mater. Chem. C* **2015**, *3*, 3422-3427.
(46) Sevy, A.; Matthew, D. J.; Morse, M. D., Bond Dissociation Energies of TiC, ZrC, HfC, ThC, NbC, and TaC. *The Journal of Chemical Physics* **2018**, *149*, 044306.
(47) Tsutsui, M., *Introduction to Metal π-Complex Chemistry*; Springer Science & Business Media, 2013.
(48) Ju, M.; Kuang, X.; Lu, C.; Li, H.; Wang, J.; Zhang, C.; Zhu, Y.; Yeung, Y., Determination of the Microstructure, Energy Levels and Magnetic Dipole Transition Mechanism for Tm^{3+} Doped Yttrium Aluminum Borate. *J. Mater. Chem. C* **2016**, *4*, 1988-1995.
(49) Su, H.-Y.; Sun, K.; Wang, W.-Q.; Zeng, Z.; Calle-Vallejo, F.; Li, W.-X., Establishing and Understanding Adsorption–Energy Scaling Relations with Negative Slopes. *J. Phys. Chem. Lett.* **2016**, *7*, 5302-5306.
(50) Li, Q.; Yin, Q.; Zheng, Y.-S.; Sui, Z.-J.; Zhou, X.-G.; Chen, D.; Zhu, Y.-A., Insights into Hydrogen Transport Behavior on Perovskite Surfaces: Transition from the Grotthuss Mechanism to the Vehicle Mechanism. *Langmuir.* **2019**, *35*, 9962-9969.

TOC Graphic

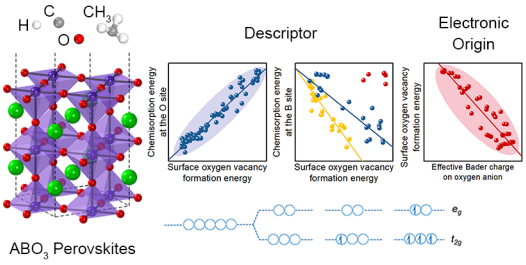
H
C
CH3
O
ABO3 Perovskites
Descriptor
Electronic Origin
Chemisorption energy at the O site
Surface oxygen vacancy formation energy
Chemisorption energy at the B site
Surface oxygen vacancy formation energy
Surface oxygen vacancy formation energy
Effective Bader charge on oxygen anion
eg
t2g